

Research Article pubs.acs.org/chemneuro

Repurposing a Cardiovascular Disease Drug of Cloridarol as hIAPP Inhibitor

Yijing Tang, Yonglan Liu, Yanxian Zhang, Dong Zhang, Xiong Gong, and Jie Zheng*



Cite This: ACS Chem. Neurosci. 2021, 12, 1419-1427

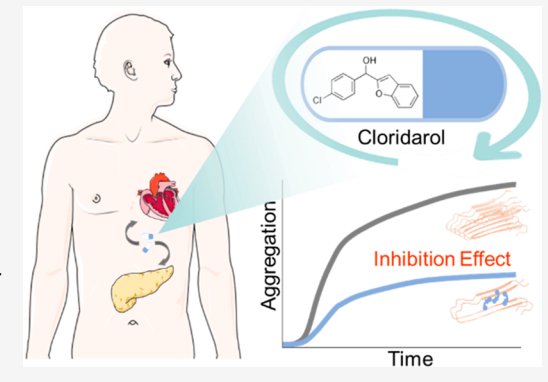


ACCESS

Metrics & More

Article Recommendations

ABSTRACT: Accumulating evidence have shown a strong pathological correlation between cardiovascular disease (CVD) and Type II diabetes (T2D), both of which share many common risk factors (e.g., hyperglycemia, hypertension, hypercoagulability, and dyslipidemia) and mutually contribute to each other. Driven by such strong CVD-T2D correlation and marginal benefits from drug development for T2D, here we proposed to repurpose a CVD drug of cloridarol as human islet amyloid peptide (hIAPP) inhibitor against its abnormal misfolding and aggregation, which is considered as a common and critical pathological event in T2D. To this end, we investigated the inhibition activity of cloridarol on the aggregation and toxicity of hIAPP₁₋₃₇ using combined experimental and computational approaches. Collective experimental data from ThT, AFM, and CD demonstrated the inhibition ability of cloridarol to prevent hIAPP aggregation from its monomeric and oligomeric states, leading to the overall reduction of hIAPP



fibrils up to 57% at optimal conditions. MTT and LDH cell assays also showed that cloridarol can also effectively increase cell viability by 15% and decrease cell apoptosis by 28%, confirming its protection of islet β -cells from hIAPP-induced cell toxicity. Furthermore, comparative molecular dynamics simulations revealed that cloridarol was preferentially bound to the C-terminal β sheet region of hIAPP oligomers through a combination of hydrophobic interactions, $\pi - \pi$ stacking, and hydrogen bonding. Such multiple site bindings allowed cloridarol to disturb hIAPP structures, reduce β -sheet content, and block the lateral association pathway of hIAPP aggregates, thus explaining experimental findings. Different from other single-target hIAPP inhibitors, cloridarol is unique in that it works as both a CVD drug and hIAPP inhibitor, which can be used as a viable structural template (especially for benzofuran) for the further development of cloridarol-based or benzofuran-based inhibitors of amyloid proteins.

KEYWORDS: Cloridarol, hIAPP, amyloid inhibitor, type II diabetes, cardiovascular disease, drug repurposing

1. INTRODUCTION

Type II diabetes (T2D) is a common chronic metabolic disease, affecting ~460 million people globally. Current prevailing "amyloid cascade hypothesis" postulates that the aggregation and misfolding of human islet amyloid peptide (hIAPP or amylin) into highly ordered, β -structure-rich species (namely amyloids) is considered as a central pathogenic cause of T2D.^{2,3} Similar to hIAPP, many other proteins including A β , α -synuclein, and prion proteins have been identified to possess self-aggregation ability to form structurally similar amyloids, which are linked to Alzheimer, Parkinson, and prion diseases. hIAPP, as a 37-residue endocrine hormone peptide (Figure 1a), is produced in the pancreatic β -cells and cosecreted with insulin, released into the bloodstream, and, finally, excreted through the kidney for both diabetic and healthy people.⁴⁻⁷ Under normal and healthy conditions, hIAPP mainly exists as nonaggregated species with disordered structures, which are proved to be nontoxic to islet β -cells^{8,9} but function as glucose regulator and glycemic controller by

slowing gastric emptying, lowering postprandial glucose, and reducing insulin release. However, under disease conditions in T2D patients, hIAPP aggregates into β -structure-rich islet amyloids in the pancreas, which induce the dysfunction and death of β -cells. Among hIAPP aggregates, hIAPP oligomers are more active and toxic to β -cells than mature fibrils. ^{10,11} Therefore, different lab-to-bench strategies have been developed to discover and design different types of inhibitors, including organic molecules, 12–15 nanoparticles, 16,17 polymers, ^{18,19} and peptides, ^{20,21} for preventing hIAPP aggregation and toxicity.²² However, almost all of newly developed hIAPP inhibitors did not achieve any clinical success, mainly because

Received: February 16, 2021 Accepted: March 17, 2021 Published: March 29, 2021





a hIAPP_{1.37} KCNTATCATQRLANFLVHSSNNFGAILSSTNVGSNTY

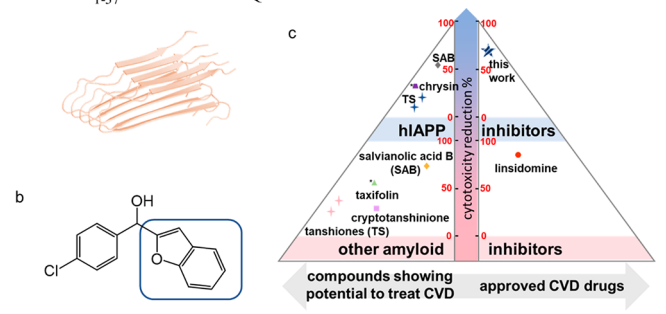


Figure 1. (a) Sequence and fibrillar U-bent, β-structure-rich structure of hIAPP. (b) Chemical structure of cloridarol with a benzofuran group that is boxed. (c) Comparison of CVD drugs used as amyloid inhibitors for their cytotoxicity reduction capacity. *No cytotoxicity data are available in references. References for these CVD drugs are listed in Table 1.

of poor biocompatibility, low binding affinity and selectivity, and low permeability across the blood-brain barrier (BBB).

Moreover, when it is taken into consideration that T2D is a complex, multifactorial, age-related syndrome, accumulating evidence also shows that cardiovascular disease (CVD), including coronary heart disease, strokes, and peripheral vascular disease, is considered as a risk factor for triggering and promoting the progression of T2Ds. 23-25 Evidently, people with CVD have a 2-4 times higher risk of developing T2D than healthy people. Additionally, T2D and CVD patients appear to share some common risk factors of hyperglycemia, hypertension, hypercoagulability, and dyslipidemia,^{28,29} implying a potential pathological link between CVD (heart protection) and T2D (sugar control). Given such close correlation between CVD and T2D and marginal benefits from developing new hIAPP inhibitors, drug repurposing strategy, particularly in the context of COVID-19, is increasingly becoming an attractive practice for searching and discovering new clinical uses of existing drugs, 30-32 simply because of several irreplaceable advantages over new drug discovery, including (i) reduction of cost, time, and steps for clinic trials, (ii) proof of having a low toxicity to the human body, (iii) well-known side effects, dosages, and possible complications, and (iv) increase of the success rate even if restarting the drug discovery process. Some studies, except a few, have reported to repurpose CVD drugs as amyloid inhibitors at lab and clinical trials (Figure 1c and Table 1).

CVD drugs of linsidomine have been discovered to prevent the aggregation and toxicity of $A\beta_{1-42}$ in vitro³³ and in vivo.³⁴ Bleomycin³⁵ and genistein¹³ have been proven to possess a dual inhibition ability against both $A\beta_{1-42}$ and hIAPP₁₋₃₇ aggregation. Similarly, salvia miltiorrhiza as a traditional Chinese herb usually used in cardiovascular disease and its components including tanshinone I, tanshinone II, ^{14,36} and cryptotanshinone ³⁷ have been discovered as $A\beta_{1-42}$ and hIAPP₁₋₃₇ inhibitors. Mutually, Metformin, an oral antidiabetic drug, has been used to treat aging, obesity, and even cancer.³⁸ More recently, tafamidis as an FDA-approved transthyretin inhibitor has been found to have a new function in the treatment of cardiomyopathy.³⁹

In this work, we propose a drug-repurpose strategy to discover a CVD drug of cloridarol 40 from Kyoto Encyclopedia of Genes and Genomes (KEGG) database⁴¹ with a new function as an hIAPP inhibitor. From a molecular structure viewpoint, cloridarol (Figure 1b) belongs to an organic compound family of benzofurans, all of which contain a benzene ring fused to a furan. Several studies have shown that the benzofuran family has been widely used in pharmacological or clinical applications for anti-inflammatory, antibacterial, antidiabetic, and antioxidant effects. 42-44 In addition, because cloridarol has a similar aromatic ring to that of the well-known amyloid inhibitor of polyphenols, such a similar structure may offer a similar structural-basis binding hypothesis for cloridarol to interfere with the β -sheet structure of hIAPP via hydrophobic and $\pi - \pi$ interactions, which in turn competitively reduce hIAPP-hIAPP interactions and thus prevent hIAPP aggregation. To test this hypothesis, we examine the inhibition activity of cloridarol on the aggregation and toxicity of fulllength hIAPP₁₋₃₇ using combined experimental and computational approaches including thioflavin (ThT) fluorescence assay, atomic force microscopy (AFM), circular dichroism (CD) spectroscopy, cell viability assay (MTT), cytotoxicity assay (LDH), and molecular dynamics (MD) simulations. Our aggregation data from ThT, AFM, and CD confirmed that cloridarol exhibited a dose-dependent inhibition property against hIAPP aggregation and toxicity via different inhibition pathways by energetically binding monomeric and oligomeric hIAPP species, delaying and disturbing the conformational change of hIAPP aggregates to β -sheet structures, and remodeling their aggregation kinetics, all of which contributed to the reduction of hIAPP-induced cell toxicity from MTT and LDH assays. MD simulations of an hIAPP pentamer in the

Table 1. Summary of CVD-Related Drugs Used as Amyloid Inhibitors

	inhibitor	amyloid	molar ratio ^a	cytotoxicity reduction ^b	ref
approved CVD drugs	cloridarol	hIAPP	5	69%	this work
	linsidomine	$A\beta$	5	83%	33
compounds showing potential to treat CVD	tanshiones I	hIAPP	0.5	28%	14
	tanshiones II	hIAPP	0.5	10%	14
	salvianolic acid B	hIAPP	5	53%	45
	chrysin	hIAPP	2	N/A	46
	tanshiones I	$A\beta$	2	43%	36
	tanshiones II	$A\beta$	2	30%	36
	salvianolic acid B	$A\beta$	2	72%	47
	cryptotanshinione	$A\beta$	0.5	40%	37
	taxifolin	$A\beta$	6	N/A	48

 $[^]a$ Minimum molar ratio of inhibitor to amyloid peptide to achieve the best inhibitory performance. b Maximum cytotoxicity reduction to be achieved in cell assays.

presence of cloridarol demonstrated strong and specific binding of cloridarol to the β -sheet structure of hIAPP through hydrophobic interactions and hydrogen bonding. After we consider a highly possible pathological link between CVD and T2D, repurposing a CVD drug of cloridarol with an hIAPP inhibition function will prevent both risk factors from vascular congestion and amyloid aggregation, thus achieving the higher drug efficiency for better treating CVD and T2D via a "kill two birds with one stone" method. In a broader view, given well-established pharmaceutical functions of cloridarol in drug delivery (nontoxic, biocompatible, nerve cell-targeting properties), cloridarol could serve as a leading structural template (especially for benzofuran) for the future development of cloridarol-based or benzofuran-based inhibitors of amyloid proteins.

2. RESULTS AND DISCUSSION

2.1. Cloridarol Inhibits hIAPP₁₋₃₇ **Fibrillization.** We first used the thioflavin T (ThT) assay to study the aggregation kinetics of hIAPP (25 μ M) in the absence and presence of cloridarol of different concentrations (25–125 μ M). In Figure 2, first, pure cloridarol as a control even at a high concentration

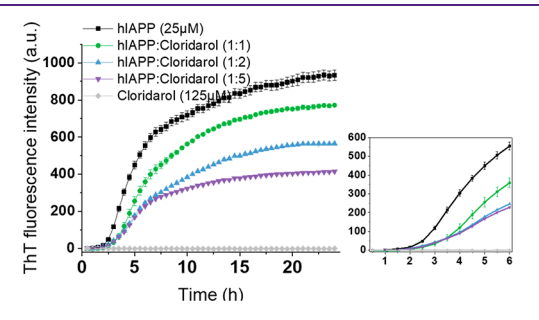


Figure 2. Time-dependent ThT fluorescence profiles for $25 \mu M$ hIAPP aggregation in the absence and presence of cloridarol at different molar ratios of hIAPP/cloridarol of 1:1, 1:2, and 1:5. The insets are enlarged views of the initial aggregation of hIAPP with and without cloridarol at a lag phase.

of 125 μ M did not produce any ThT signal, thus eliminating the possibility of cloridarol for interfering with ThT intensity. Second, pure hIAPP (25 µM) exhibited a ypical sigmoidal growth curve (i.e, nucleation-polymerization aggregation), starting with a lag phase within 2 h and followed by a rapid growth phase until 20 h; then, it finally achieved a stable plateau with a ThT intensity of ~783 au. For comparison, when there was incubation of cloridarol with freshly dissolved hIAPP monomers at different molar ratios from 1:1 to 1:5, hIAPP aggregation kinetics showed dramatic decrease at all aggregation stages in a dose-dependent manner, as evidenced by (i) the increase of lag time from 2 h to 3 h, (ii) the slowing down of the aggregate rate at the growth phase, and (iii) the reduction of final ThT intensity at the equilibrium phase. Specifically, cloridarol exhibited obvious inhibitory performance by decreasing the final ThT fluorescence by 17.3, 39.4, and 55.6% as the hIAPP/cloridarol molar ratio increased from 1:1 to 1:5, confirming the dose-dependent inhibition behavior of cloridarol. Additionally, as cloridarol concentration was higher than 50 μ M, ThT curves were largely overlapped at the lag period and growth phases, indicating that the cloridarolinduced inhibitory effect on hIAPP aggregation reached saturation.

2.2. Cloridarol Modifies the Morphologies and Secondary Structures of hIAPP $_{1-37}$. To better understand how the cloridarol-induced conformational change of hIAPP is correlated with the cloridarol-induced inhibition of hIAPP aggregation, we further monitored the morphological and secondary structure changes during hIAPP (25 μ M) aggregation in the presence of cloridarol (125 μ M) using AFM and CD. As shown in the first row of Figure 3, incubation

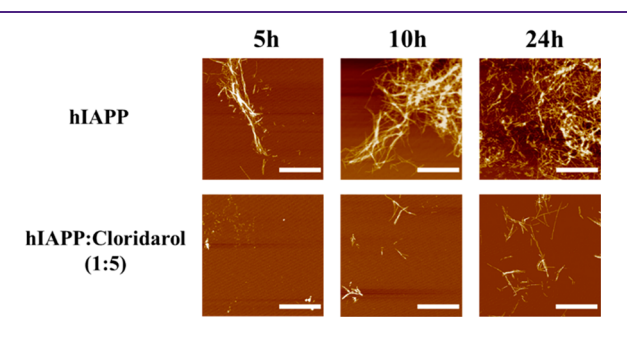


Figure 3. AFM images for hIAPP (25 μ M) in the absence (first row) and presence of cloridarol (125 μ M, second row) at 5, 10, and 24 h. Scale bars are 1 μ m.

of pure hIAPP (25 μ M) for 5 h already produced a large amount of short fibrils that were stacked together and had the average length of ~300 nm. Upon 10 h incubation, these short fibrils gradually grew into more and longer protofibrils, with average heights of ~30 nm. At 24 h, dense clusters of thick mature fibrils were formed, consistent with the fluorescence plateau at 24 h in the ThT assay. For comparison, coincubation of hIAPP with cloridarol at hIAPP/cloridarol of 5 h dramatically slowed down or inhibited the hIAPP aggregation process. Even after 10 h, protofibrils were absent with some globular aggregates (~200 nm), while at 24 h, only few scattered thin fibrils (~10 nm in height) were observed. Quantitively, the amount of fibrils formed by the hIAPP/ cloridarol (1:5) system at 24 h was comparable with that of the pure hIAPP system at 5 h, in agreement with similarly low ThT intensity as recorded for both hIAPP/cloridarol at 24 h (~414 au) and pure hIAPP at 5 h (~449 au). AFM and CD data confirm the inhibition ability of cloridarol to retard the hIAPP fibrillization.

Next, we used CD spectroscopy to monitor the secondary structure changes of hIAPP (25 μ M) with and without cloridarol (125 μ M). To be consistent with ThT and AFM tests, we used the same time points of 0, 5, 10, and 24 h to cover the lag, growth, and equilibrium phases off hIAPP aggregation. In Figure 4a, hIAPP (25 µM) alone displayed a typical structural transition, starting from random coli as signified by the negative peak at \sim 198 nm to the α -helix (negative peak at ~208 and ~222 nm) at 5 h and, finally, to the characteristic cross β -sheet structure (negative peak at ~215 nm). For comparison, when cloridarol was added to hIAPP fresh solution at a molar ratio of 5, the entire structural transition was delayed at all time points (Figure 4b). At the beginning of coincubation of hIAPP and cloridarol, CD spectra showed a sole and strong negative peak at about 197 nm, indicative of (i) the random coil structure of the mixed sample and (ii) no CD interference by cloridarol. At 5 h of coincubation, a mixture of hIAPP and cloridarol still adopted random coil structure, showing the slower aggregation kinetics than that of pure hIAPP whose curve has moved to ~215 nm

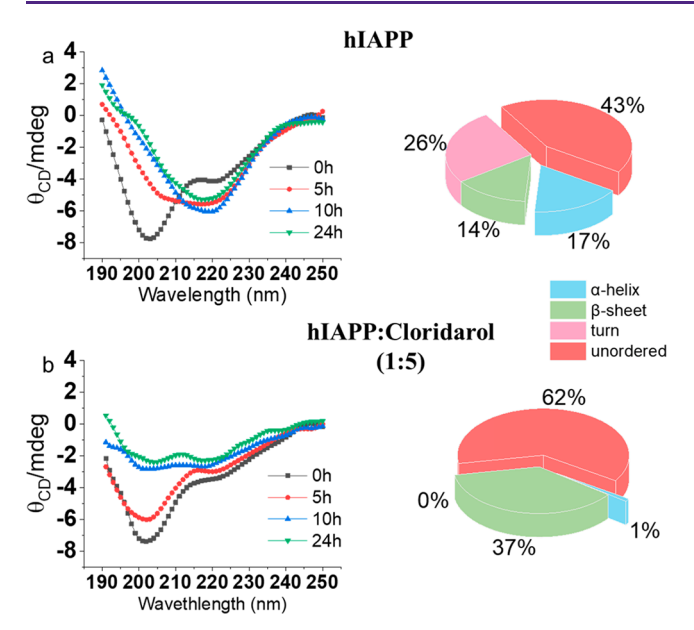


Figure 4. Time-dependent circular dichroism (CD) spectra and secondary structure distributions of (a) pure hIAPP ($25 \mu M$) and (b) the mixture of hIAPP–cloridarol ($25 \mu M$:125 μM) for 24 h.

at 5 h. After 24 h, while characteristic β -sheet-pertaining peaks at ~198 to ~215 nm started to appear, both peaks were greatly reduced in their intensities and also coexisted with the peaks of random coils. Considering that conformational changes from a random coil/ α -helix to a β -sheet structure is the crucial step for the formation of cross β -sheets and fibrillogenesis of hIAPP, we further analyzed the secondary structure contents of both pure hIAPP and a mixture of hIAPP-cloridarol at 24 h. Quantitively, pure hIAPP adopted 40% of the β -structure, 17% of the α -helix, and 43% of the random coils, while the cloridarol-treated hIAPP sample contained a majority of the random coils (62%) and 37% of the β -structure. Clearly, cloridarol converted α -helical structures to random structures, thus abolishing the hIAPP aggregation pathways from α -helix to β -sheet. ⁴⁹ Again, in line with the ThT and AFM results, the changes in CD spectra confirm the ability of cloridarol to inhibit hIAPP fibrillization by especially hindering the conformational change of hIAPP from random coil to α helix, thus influencing hIAPP fibril formation.

2.3. Cloridarol Exhibits Different Inhibitory Performances by Remodeling Different Aggregation Pathways of hIAPP₁₋₃₇. While cloridarol exhibited its strong inhibition ability to prevent hIAPP aggregation from monomers to fibrils (Figure 2), it is also fundamentally interesting and important to examine whether cloridarol could also inhibit hIAPP aggregation from preformed hIAPP seeds. To address this issue, we designed a new type of seeding experiments by incubating cloridarol (125 µM) with different hIAPP seed solutions (25 μ M) obtained from 1 h lag, 5 h growth, and 11 h equilibrium phases, followed by the tests for inhibitory efficiency by monitoring the aggregation kinetics changes (i.e., ThT signals) before and after adding cloridarol to hIAPP seed solutions. As shown in Figure 5a, at the first glance, addition of cloridarol (125 μ M) to three different hIAPP seed solutions led to different inhibition scenarios. Specifically, when cloridarol was added to 1 h hIAPP seed solution at a lag phase, the ThT aggregation kinetics curve (pink curve) was almost the same as the addition of cloridarol to freshly

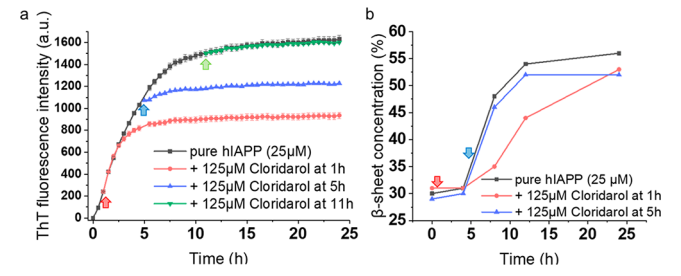


Figure 5. Inhibition effect of cloridarol on the aggregation of preformed hIAPP seeds. Time-dependent (a) ThT aggregation kinetics and (b) β-sheet contents by adding 125 μM cloridarol to different hIAPP seed solutions (25 μM) preformed at 1, 5, and 11 h.

prepared hIAPP solution (black curve) within 2.5 h. After that, further hIAPP aggregation was immediately inhibited and quickly reached to a stable plateau of ~935, showing a 42.7% decrease of final fibril formation. Differently, addition of cloridarol to 5 h hIAPP seeds showed an immediate stop of the growth of hIAPP aggregation, resulting in a largely reduced final ThT intensity of ~1228 (blue curve), equivalent to 24.8% of fibril reduction as compared to final ThT intensity of coincubation of cloridarol with hIAPP monomers (black curve). In sharp contrast to these two inhibition scenarios, when adding cloridarol to the preformed hIAPP fibrils at 11 h, no inhibition effect was observed, as indicated by no decrease of final fibril amounts in the ThT curve (green curve). In parallel, we quantified the secondary structure changes of hIAPP when adding cloridarol (125 μ M) to different hIAPP seed solutions preformed at 1 and 5 h. Consistent with ThT results, β -sheet content in Figure 5b confirmed the inhibitory performance of cloridarol on both 1-h- and 5-h-seeded hIAPP solutions, as evidenced by the lower β -sheet content after adding cloridarol. Specifically, the β -content was largely reduced by up to 13% for the cloridarol/1-h-seeded hIAPP system and 4% for the cloridarol/5-h-seeded hIAPP system at a growth phase, respectively, as compared to that of pure

Both ThT and CD data from the seeding experiments indicate that cloridarol is more effective to inhibit the aggregation and conversion of hIAPP species formed at the early lag and growth phase but loses its inhibition ability if high-ordered hIAPP protofibrils or fibrils are formed. This also indicates that cloridarol lacks the ability to disintegrate preformed hIAPP fibrils, which has also been confirmed by our disassembling hIAPP fibril tests by cloridarol (data not shown). On the other hand, while cloridarol has no effect on either the inhibition or disassembly of the preformed hIAPP fibrils, cloridarol could still preserve its inhibitory ability to selectively bind to the low-ordered hIAPP aggregates (monomers and oligomers) available in the seed solution (as confirmed by the first two inhibition scenarios), thus hindering their self-aggregation.

2.4. Cloridarol Reduces hIAPP_{1–37}-Induced Cytotoxicity. To determine whether cloridarol could protect cells from hIAPP-induced toxicity, we applied 3-(4,5-dimethylthiazole-2-yl)-2,5-diphenyltetrazolium bromide (MTT) and lactate dehydrogenase (LDH) assays to examine the potential protection role of cloridarol in pancreatic cells using the RIN-m5F cell line for 24 and 48 h. Three controls were conducted and used as baselines for comparison. RIN-m5F cells incubated without any treatment were used as control,

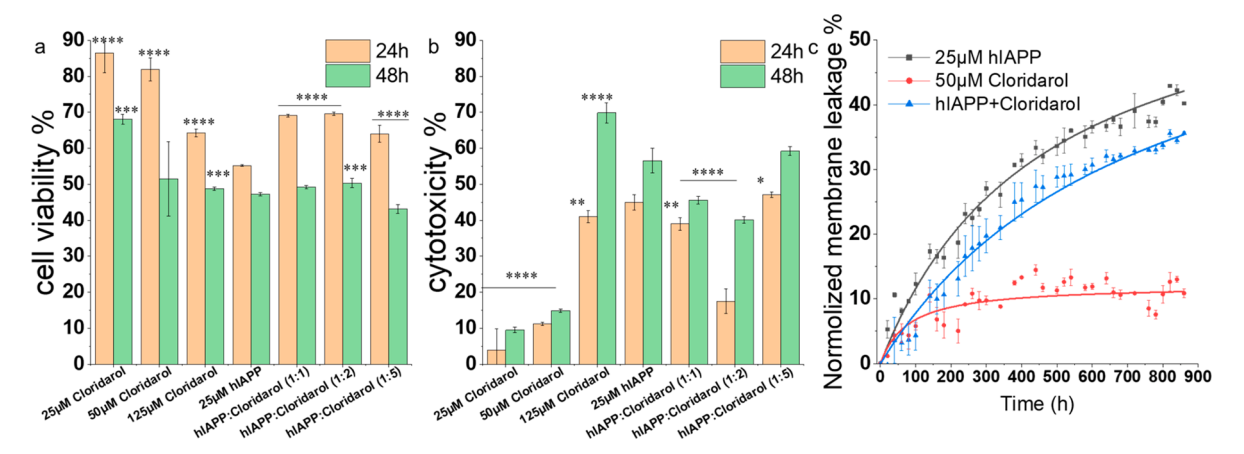


Figure 6. (a) MTT assay for cell viability and (b) LDH assay for cell apoptosis for incubation of hIAPP (25 μ M) with and without cloridarol at molar ratios of 1:1, 1:2, and 1:5 during 24 and 48 h incubation. Data were normalized by the pure cell group. (c) The hIAPP-induced membrane leakage in the absence and presence of cloridarol at an hIAPP: cloridarol molar ratio of 1:2 (25 μ M:50 μ M). Data represent mean \pm SD of three independent experiments (n = 3).

and their viability was set as 100%. RIN-m5F cells cocultured with pure hIAPP (25 μ M) exhibited 55 and 47% cell viability (Figure 6a) and 45 and 56% cell apoptosis (Figure 6b) during 24 and 48 h incubation time, showing high cell cytotoxicity as induced by hIAPP. Pure cloridarol showed the concentrationand time-dependent cytotoxicity; i.e., at 24 h, cloridarol-caused cell viability was reduced from 86 to 64%, while its cytotoxicity increased from 3 to 41% as cloridarol concentration increased from 25 to 125 μ M. Extension of incubation time from 24 to 48 h further decreased cell viability to 68–48% and increased cytotoxicity to 9–69%. Clinically, a 250 mg capsule containing cloridarol (3 times per day⁴⁰) has been shown to have a positive effect for treating CVD, which could serve as a reference for future development of cloridarol as a T2D drug.

In parallel, when incubating all of RIN-m5F cells, hIAPP, and cloridarol together for 24 h, cell viability/cell apoptosis was 69%/38%, 70%/17%, and 64%/47% at hIAPP:cloridarol ratios of 1:1, 1:2, and 1:5, respectively (Figure 6a,b). The further increase of incubation time to 48 h resulted in a decrease of ~20% in cell viability and an increase of about 7–23% in apoptosis for all the samples cotreated with cloridarol. Overall, both MTT and LDH results unambiguously evidenced that cloridarol at an optimal concentration of 50 μ M can effectively alleviate hIAPP-mediated β -cell toxicity. Too high or too low concentrations led to the reduction of cell toxicity inhibition to some extents. Thus, the overall cell toxicity is a result of the competition between cloridarol-inhibition-induced cell protection and both cloridarol- and hIAPP-caused cell damage.

Furthermore, we coincubated large unilamellar vesicles (LUVs) with hIAPP in the absence and presence of cloridarol to examine whether cloridarol could reduce the hIAPP-induced membrane leakage, which help to explain the protective ability of cloridarol on hIAPP-induced cell apoptosis. Carboxyfluorescein dye was preloaded into the interior of LUVs made of DOPC and DOPS lipids, in which carboxyfluorescein was self-quenched. Any membrane disruption of LUVs will cause carboxyfluorescein to leak into the solution and lead to the enhanced fluorescent emission, thus acting as an indicator for quantifying the extent of membrane leakage. In Figure 6c, upon incubation of 50 μ M cloridarol with LUVs for 15 h, very minor membrane leakage of <10% was observed, also indicating that 50 μ M cloridarol is a safe

concentration. In sharp contrast, 25 μ M hIAPP alone induced a rapid and significant membrane leakage from 0 to 31% as the incubation time increased from 0 to 400 min. It can be seen that, even after 900 min, this increasing trend still remained. It was evident that addition of cloridarol (50 μ M) to hIAPP solution can not only slow down the membrane leakage but also reduce hIAPP-induced membrane leakage by 19%. Importantly, side-by-side comparison of membrane leakage curves (Figure 6c) with the ThT curve (Figure 2) reveals that the membrane disruption timeline is well aligned with the growth phase of hIAPP aggregation; i.e., hIAPP oligomers formed at the early lag and growth stages (0-15 h) are the main species to induce membrane leakage and thus cell toxicity. Taken together, MTT, LDH, and LUV data confirm the protective role of cloridarol in inhibiting hIAPP aggregation and hIAPP-induced membrane leakage, both of which account for the reduced cell toxicity.

2.5. MD Simulations Reveal the Interactions between Cloridarol and hIAPP. Strong inhibition property of cloridarol against hIAPP aggregation and toxicity is speculated to stem from strong cloridarol-hIAPP interactions. To better understand the cloridarol-binding-induced inhibition of hIAPP, we performed molecular dynamics (MD) simulations to explore possible binding modes of cloridarol to an hIAPP pentamer, which was experimentally identified as highly populated aggregate species. 50,51 Based on our aggregation and toxicity assays, cloridarol achieved the best inhibition performance against both hIAPP aggregation and toxicity at a molar ratio of cloridarol:hIAPP = 2. We constructed a cloridarol-hIAPP system by randomly placing ten cloridarol molecules around an hIAPP pentamer with the separation distances of 5-8 Å between them (Figure 7a). Visual inspection of MD trajectories showed that, during 80 ns simulations, cloridarol consistently binded to the hIAPP pentamer. While such strong cloridarol binding caused some loss of structural integrity as indicated by twists between adjacent β -strands, parallel β -strands and the U-shaped peptide topology in the hIAPP pentamer were still maintained, without peptide dissociation from hIAPP pentamer. Furthermore, comparison of root-mean-square deviation (RMSD) and β structure content of hIAPP pentamer in the absence and presence of cloridarol also confirmed the cloridarol-induced structural disturbance of the hIAPP pentamer; i.e., cloridarol-

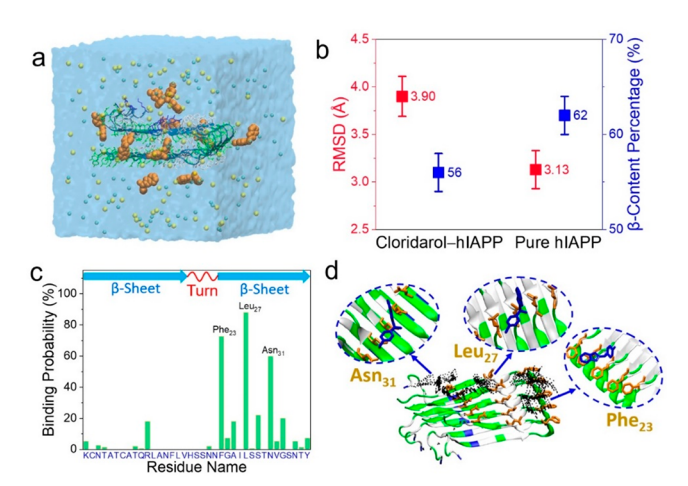


Figure 7. Molecular dynamics simulations of binding modes between cloridarol and the hIAPP pentamer. (a) Representative MD model of 10 cloridarol molecules (orange) around an hIAPP pentamer in the presence of water (blue box) and counterions of NaCl (small spheres). (b) Comparison of RMSD and β-content of the hIAPP pentamer in the absence and presence of cloridarol. (c) Binding probability (%) of chloride to each residue of hIAPP based on the chloride—residue interaction distributions. (d) Overall binding distribution and specific binding sites (Phe₂₃, Leu₂₇, and Asn₃₁) of chloride to the hIAPP pentamer.

bound hIAPP pentamer (RMSD of \sim 3.90 Å and β -content of 56%) displayed the higher RMSD values (i.e., the larger structural instability) and the β -content that is less than that of the pure hIAPP pentamer (RMSD of \sim 3.13 Å and β -content of 62%) (Figure 7b).

To gain insight into the specific binding sites of cloridarol to hIAPP, we analyzed the binding probability (%) of cloridarol to each residue of hIAPP based on the cloridarol-residue interactions. At the first glance, in Figure 7c, cloridarol exhibited inhomogeneous binding to hIAPP residues, indicating that cloridarol has more favorable binding to some specific residues of hIAPP. After we used a cutoff value of -20 kcal/mol to define the strong and weak binding of cloridarol to hIAPP residues, cloridarol evidently displayed high binding probabilities to Phe₂₃ (73%), Leu₂₇ (88%), and Asn₃₁ (60%) from the C-terminal β -sheet of hIAPP. Visually, Figure 7d shows the binding distribution of cloridarol around hIAPP with a separation distance of <4 Å, another indicator of strongbinding-induced close contacts. It can be seen clearly that cloridarol had consistent and preferential bindings to Cterminal β -sheet region, especially two hydrophobic residues of Phe23 and Leu27 and one hydrophilic residue of Asn31, which offered a combination of hydrophobic interactions, $\pi - \pi$ stackings, and hydrogen bondings to strengthen the cloridarol-hIAPP bindings. Moreover, the binding of cloridarol to the C-terminal β -sheet region allows for the hIAPP aggregation pathway to be blocked via lateral association. Similar binding preferences of other organic molecules to the β -sheet groove of $A\beta$, a general signature of amyloid fibrils, have also been observed, 13,14 suggesting a common binding-induced amyloid inhibition mechanism by targeting β -sheet-rich structures to prevent amyloid-amyloid interactions from their self-aggregation.

3. CONCLUSIONS

Given accumulating evidence for implying a close pathological relation between CVD and T2D, we propose a drugrepurposing strategy to discover a CVD drug of cloridarol with a new hIAPP₁₋₃₇ inhibition function. Collective aggregation data from ThT assays, AFM images, and CD spectra confirmed that cloridarol exhibited a dose-dependent inhibition property against hIAPP fibrillogenesis, leading to a maximal reduction of fibril formation by 55.6% as compared to that of pure hIAPP-formed fibrils. Seeding experiments further revealed that cloridarol induced such strong hIAPP inhibition via the two main pathways by binding to (i) hIAPP monomers to prevent the conformational changes from random coils/ α helixes to β -structure at a lag phase and (ii) hIAPP oligomers to prevent hIAPP-hIAPP associations at the early growth phase. Biologically, in vitro cell assays showed that cloridarol can rescue islet RIN-m5F cells from the hIAPP-induced toxicity, as evidenced by the increase of cell viability from 55 to 70% and the decrease of cell apoptosis from 44 to 17% at an optimal cloridarol:hIAPP ratio of 2:1. In parallel, MD simulations further provided molecular insights into an hIAPP inhibition mechanism about the interactions between cloridarol and hIAPP. Cloridarol had a more preferential and stronger interaction with the C-terminal β -sheets of hIAPP oligomers through a combination of hydrophobic interactions, π - π stacking, and hydrogen bonding, which allow cloridarol to disturb hIAPP structure and β -structure content, weaken the hIAPP-hIAPP interaction, and block the hIAPP lateral association pathway. This work again provides a new strategy to search for amyloid inhibitors from CVD drugs, which could be more effective for both CVD and T2D treatments by blocking multipathologically linked targets. In a broader view, considering huge societal and drug-development costs to treat T2D patients, drug-repurposing strategy allows for the research of a new amyloid inhibition function of many existing drugs so as to avoid many potential pitfalls in drug discovery for amyloid diseases.

4. METHODS

- **4.1. Materials.** Human islet amylin (hIAPP, ≥95%) was purchased from CPC Scientific (CA, USA). Cloridarol (95%) was purchased from Enamine (Kiev, Ukraine.). The 1,1,1,3,3,3-hexafluoro-2-propanol (HFIP, ≥99.9%), dimethyl sulfoxide (DMSO, ≥99.9%), and thioflavin T (ThT, 98%) were purchased from Sigma-Aldrich (St. Louis, MO). 1,2-Dioleoyl-sn-glycero-3-phosphocholine (DOPC, ≥97.0%) was purchased from TCI America (Portland, OR). 1,2-Dioleoyl-sn-glycero-3-phospho-L-serine (DOPS, ≥99.0%) was purchased from Avanti Polar Lipids (Alabaster, AL).
- **4.2. Peptide Preparation.** Human islet amylin (hIAPP $_{1-37}$) was purchased in lyophilized form and stored at $-20~^{\circ}$ C immediately on arrival. To break pre-existing hIAPP $_{1-37}$ aggregations and seeds to obtain the monomer, 1.0 mg of hIAPP $_{1-37}$ was dissolved in 1 mL of HFIP and incubated at room temperature for 2 h; then, it was sonicated in an ice bath for 30 min and centrifuged at 14 000 rpm and 4 $^{\circ}$ C for 30 min. Finally, supernatant was aliquoted into different subpackages according to experimental need and stored at $-80~^{\circ}$ C. To obtain the monomeric hIAPP $_{1-37}$ stock solution, subpackaged peptides were lyophilized using a freeze-dryer for more than 30 min before solubilized in 10 mM NaOH and diluted in different buffer to achieve the concentration of 25 μ M.
- **4.3. Thioflavin T (ThT) Fluorescence Assay.** ThT powder was dissolve into Milli-Q water to a concentration of 2 mM and then stored in a dark place at room temperature. The stock solution was then sonicated to a particle-free state and diluted in Tris buffer to $10 \mu M$. Samples were prepared by mixing hIAPP₁₋₃₇ with and without

cloridarol (25–125 μ M) to achieve total test volume of 200 μ L. The kinetic bottom-read mode of a SpectraMax M3 microplate reader (Molecular Devices, CA, USA) was used to obtain the fluorescence spectra with excitation at 450 nm and emission at the range 470–500 nm. All the ThT fluorescence experiments were conducted in triplicate.

4.4. Circular Dichroism (CD) Spectroscopy. A total volume of 600 μ L of hIAPP₁₋₃₇/cloridarol/hIAPP₁₋₃₇-cloridarol samples was incubated at 37 °C in 10 mM phosphate-buffered saline (PBS, pH 7.4) for a different time period. Samples (150 μ L) were pipetted into a 1 mm optical path length CD cuvette and measured by using a J-1500 spectropolarimeter (Jasco Inc., Japan) at room temperature. The spectra of the solution samples were recorded between 190 and 250 at 0.5 nm resolution and 50 nm/min scan rate. To remove the background influence, all spectra were analyzed by subtracting the PBS buffer baseline. The secondary structure concentration of each sample was determined by using a self-consistent method (CDSSTR program) in the CDPro analysis software.

4.5. Atomic Force Microscopy (AFM). The morphology changes of hIAPP $_{1-37}$ mediated by cloridarol were characterized by using Nanoscope III multimode AFM with an Extender eletroncis module (Veeco Corp, Santa Barbara, CA) in a ScanAsyst Mode. The hIAPP $_{1-37}$ in the presence and absence of 125 μ M cloridarol was incubated in 10 mM PBS buffer, and 20 μ L samples at different time points were dropped on a piece of cleaved mica for 5 min, rinsed three times with Mill-Q water to totally remove additional salt, and dried with an air stream before they were stored in a sealed container. All images were recorded at the 512 pixel \times 512 pixel resolution at a typical scan rate of 1.0 Hz and with the vertical tip oscillation frequency of 250–350 kHz. Representative AFM images were obtained by scanning six different locations on the mica surface.

4.6. Cell Culture. Rat insulinoma cells RIN-mSF (ATCC CRL-11605TM, VA, USA) were incubated in sterile-filtered RPMI-1640 medium mixed with 10% (v/v) FBS and 1% (v/v) penicillin/streptomycin at 37 °C and 5% CO₂ in a humidified incubator. Cells were incubated in a T75 flask until there was cell coverage for over 80% of the surface area, and they were harvested by using 0.25 mg/mL Trypsin/EDTA solution (Sigma-Aldrich). Cells were then plated in a 96-well cell culture plate with 2 × 10⁴ cells per well in 100 μ L of cell culture medium and incubated 24 h for cell attachment.

4.7. MTT Assay. RIN-m5F cells were seeded in 96-well plates ($2 \times$ 10⁴ per well) for 24 h before MTT and LDH assays. After removing culture medium, fresh cell culture medium with hIAPP₁₋₃₇/ cloridarol/hIAPP₁₋₃₇-cloridarol solutions were separated and added into wells, followed by culture of the cells for 24 and 48 h at 37 °C and 5% CO₂ in a humidified incubator. In the MTT experiment, 5 mg of 3-(4,5-dimethylthiazole-2-yl)-2,5-diphenyltetrazolium bromide (MTT) was first dissolved in 1 mL of PBS buffer; then, 9 mL of culture medium was added to obtain the MTT kit solution for further use. The culture medium was discarded, and 100 μ L of MTT kit solution was added to each well and incubated at 37 °C. After 4 h, we replaced the medium with 150 μ L of DMSO to dissolve the formazan crystals. Lastly, absorbance was recorded at 540 nm using the SpectraMax M3 microplate reader. Each sample was repeated at least six times, and cell viabilities were calculated in comparison with those of untreated cells.

4.8. LDH Assay. The cytotoxicity of amyloid peptides causing membrane leakage could be quantified by lactate dehydrogenase (LDH) assay. LDH assay was performed using CytoSelect LDH Cytotoxicity Assay Kit (Cell Biolabs, San Diego, USA). Briefly, $10~\mu L$ of sterile water (as positive control) or Triton X-100 solution (as negative control) was added to each corresponding well. After 10 min incubation at room temperature, $90~\mu L$ of medium from each well was transferred to a clean 96-well plate. Then, $10~\mu L$ of LDH cytotoxicity assay reagent was added to every well and further incubated at $37~^{\circ}C$ and $5\%~CO_2$ for 30~min. Finally, read the absorbance at 450~mm by using a SpectraMax M3 microplate reader. Relative cytotoxicity percentages were proportionally normalized by the difference of positive and negative control.

4.9. Large Unilamellar Vesicles (LUVs). LUVs were prepared at a total lipid concentration of 20 mM by dissolving DOPC, and DOPS was in chloroform and mixed in a 7:3 molar ratio. Mixtures were then evaporated with air gas and kept in a high-vacuum oven for at least 1 h to completely remove the residual organic solvent. The resulting lipid mixture were dissolved in Tris buffer [10 mM Tris—HCl and 100 mM NaCl (pH 7.4)] containing saturated 5(6)-carboxyfluorescein to reach the concentration of 2 mM. The lipid solution was then subjected to ten freeze—thaw cycles and passed through 200 nm pore size filters 10 times to obtain a uniform vesicle size. Dynamic light scattering (DLS) was used to check the effective diameter and polydispersity of each vesicle before use. A fresh LUV solution was used for each experiment.

4.10. Membrane Permeability Assays. The membrane leakage experiment was conducted using top-read mode of a SpectraMax M3 microplate reader with excitation at 485 nm and emission at 535 nm, respectively. All the samples were incubated in a 96-well quartz microplate at room temperature. The maximal leakage for totally disrupted membranes was measured by adding the detergent Triton X-100 to a final concentration of 0.05% (v/v), and pure 5(6)carboxyfluorescein encapsulated LUV solution was set as background signal. The hIAPP₁₋₃₇ (25 μ M) monomer was added in the presence or absence of 50 μ M cloridarol to 2 mM 5(6)-carboxyfluorescein encapsulated LUVs (10 mM Tris-HCl, 100 mM NaCl, pH 7.4) solution and continuously measured during the course of each experiment. The release of the fluorescent dye was calculated as the percent fluorescence change L(t) = (Ft - Fbaseline)/(Fmax - Fbaseline)Fbaseline), where L(t) represents the normalized membrane leakage, Ft was the measured fluorescence intensity at time t, Fbaseline was the fluorescence intensity of untreated encapsulated LUV solution, and Fmax was experimentally determined by disrupting the vesicles with 0.05% (v/v) Triton X-100.

4.11. Molecular Modeling and MD Simulation Protocol. We performed MD simulations to investigate the binding and interaction of cloridarol with hIAPP. The force field of cloridarol was built using CGenFF (https://cgenff.paramchem.org/), which is compatible with the CHARMM force field.⁵² An hIAPP₁₋₃₇ pentamer was used to model the protein. The initial coordinates of the hIAPP₁₋₃₇ pentamer with a double-layer fibril-like structure was kindly provided by Tycko's group.⁵³ The force field parameter and topological information of the hIAPP are obtained from the CHARMM27 force field with CMAP correction. We constructed an hIAPP-cloridarol complex by randomly placing 10 cloridarol molecules with different orientations around an hIAPP pentamer with a separation distance of 5-8 Å between cloridarol and the protein. Then, the resultant hIAPPcloridarol complex was subjected to be solvated using the TIP3P water model, where van der Waals (VDW) potentials of both hydrogen and oxygen atoms are supposed to be calculated. Furthermore, counterions of Na+ and Cl- were added into the resulting system to mimic ionic strength of ~150 mM at a physiological condition.

Prior to production of MD simulations, the resulting hIAPPcloridarol system (Figure 7a) was first subjected to energy minimization using the 5000-step conjugate gradient minimization method. After that, 80 ns all-atom MD simulations for the system were performed using NAMD 2.13 package⁵⁴ with the NPT ensemble (constant number to atoms, pressure, and temperature) under a 3D periodic condition. During MD simulations, the temperature and pressure were maintained at 310 K and 1 atm using the Langevin thermostat method with a damping coefficient of 1 ps⁻¹ and the Langevin piston control algorithm, respectively. The RATTLE method was applied to constrain all covalent bonds, including hydrogel bonds, so that the velocity Verlet algorithm was used to integrate the Newton motion equation with a larger time step of 2 fs. The interaction potentials between atoms were estimated by longrange electrostatic interactions calculated by the particle mesh Ewald (PME) method with a grading space of 1.0 Å and short-range van der Waal interactions computed by switching functions with the twinrange cutoff at 12 and 14 Å. All MD trajectories were saved each 2 ps for further data analysis. The analysis of MD simulation results was conducted in the VMD package with in-house TCL scripts.

AUTHOR INFORMATION

Corresponding Author

Jie Zheng — Department of Chemical, Biomolecular, and Corrosion Engineering, The University of Akron, Ohio 44325, United States; orcid.org/0000-0003-1547-3612; Email: zhengj@uakron.edu

Authors

- Yijing Tang Department of Chemical, Biomolecular, and Corrosion Engineering, The University of Akron, Ohio 44325, United States
- Yonglan Liu − Department of Chemical, Biomolecular, and Corrosion Engineering, The University of Akron, Ohio 44325, United States; orcid.org/0000-0001-5280-5992
- Yanxian Zhang Department of Chemical, Biomolecular, and Corrosion Engineering, The University of Akron, Ohio 44325, United States; Department of Polymer Engineering, The University of Akron, Ohio 44325, United States
- Dong Zhang Department of Chemical, Biomolecular, and Corrosion Engineering, The University of Akron, Ohio 44325, United States; Department of Polymer Engineering, The University of Akron, Ohio 44325, United States; orcid.org/0000-0001-7002-7661
- Xiong Gong Department of Polymer Engineering, The University of Akron, Ohio 44325, United States; orcid.org/0000-0001-6525-3824

Complete contact information is available at: https://pubs.acs.org/10.1021/acschemneuro.1c00091

Author Contributions

Y.T., Y.L., and J.Z. designed the research.Y.T. and Y.Z. carried out the experiments. Y.L. and D.Z. carried out the simulations. All authors participated in data analysis, result discussion, and paper writing.

Notes

The authors declare no competing financial interest.

ACKNOWLEDGMENTS

We are thankful for financial support from NSF (2107619).

REFERENCES

- (1) Khan, M. A. B., Hashim, M. J., King, J. K., Govender, R. D., Mustafa, H., and Al Kaabi, J. (2020) Epidemiology of type 2 diabetes—global burden of disease and forecasted trends. *Journal of epidemiology and global health* 10 (1), 107.
- (2) Jaikaran, E. T., and Clark, A. (2001) Islet amyloid and type 2 diabetes: from molecular misfolding to islet pathophysiology. *Biochim. Biophys. Acta, Mol. Basis Dis.* 1537 (3), 179–203.
- (3) Saeedi, P., Petersohn, I., Salpea, P., Malanda, B., Karuranga, S., Unwin, N., Colagiuri, S., Guariguata, L., Motala, A. A., Ogurtsova, K., et al. (2019) Global and regional diabetes prevalence estimates for 2019 and projections for 2030 and 2045: Results from the International Diabetes Federation Diabetes Atlas. *Diabetes Res. Clin. Pract.* 157, 107843.
- (4) Kautzky-Willer, A., Thomaseth, K., Pacini, G., Clodi, M., Ludvik, B., Streli, C., Waldhäusl, W., and Prager, R. (1994) Role of islet amyloid polypeptide secretion in insulin-resistant humans. *Diabetologia* 37 (2), 188.
- (5) Leckström, A., Björklund, K., Permert, J., Larsson, R., and Westermark, P. (1997) Renal elimination of islet amyloid polypeptide. *Biochem. Biophys. Res. Commun.* 239 (1), 265–268.

- (6) Westermark, P., Wernstedt, C., Wilander, E., Hayden, D. W., O'Brien, T. D., and Johnson, K. H. (1987) Amyloid fibrils in human insulinoma and islets of Langerhans of the diabetic cat are derived from a neuropeptide-like protein also present in normal islet cells. *Proc. Natl. Acad. Sci. U. S. A.* 84 (11), 3881–3885.
- (7) Clark, A., Lewis, C., Willis, A., Cooper, G., Morris, J., Reid, K., and Turner, R. (1987) Islet amyloid formed from diabetes-associated peptide may be pathogenic in type-2 diabetes. *Lancet* 330 (8553), 231–234.
- (8) Zhang, M., Hu, R., Chen, H., Chang, Y., Gong, X., Liu, F., and Zheng, J. (2015) Interfacial interaction and lateral association of cross-seeding assemblies between hIAPP and rIAPP oligomers. *Phys. Chem. Chem. Phys.* 17 (16), 10373–10382.
- (9) Kapurniotu, A. (2001) Amyloidogenicity and cytotoxicity of islet amyloid polypeptide. *Biopolymers 60* (6), 438–459.
- (10) Selkoe, D. J. (2003) Folding proteins in fatal ways. *Nature* 426 (6968), 900–904.
- (11) Lorenzo, A., Razzaboni, B., Weir, G. C., and Yankner, B. A. (1994) Pancreatic islet cell toxicity of amylin associated with type-2 diabetes mellitus. *Nature* 368 (6473), 756–760.
- (12) Meng, F., Abedini, A., Plesner, A., Verchere, C. B., and Raleigh, D. P. (2010) The flavanol (–)-epigallocatechin 3-gallate inhibits amyloid formation by islet amyloid polypeptide, disaggregates amyloid fibrils, and protects cultured cells against IAPP-induced toxicity. *Biochemistry* 49 (37), 8127–8133.
- (13) Ren, B., Liu, Y., Zhang, Y., Cai, Y., Gong, X., Chang, Y., Xu, L., and Zheng, J. (2018) Genistein: a dual inhibitor of both amyloid β and human islet amylin peptides. *ACS Chem. Neurosci.* 9 (5), 1215–1224.
- (14) Ren, B., Liu, Y., Zhang, Y., Zhang, M., Sun, Y., Liang, G., Xu, J., and Zheng, J. (2018) Tanshinones inhibit hIAPP aggregation, disaggregate preformed hIAPP fibrils, and protect cultured cells. *J. Mater. Chem. B* 6 (1), 56–67.
- (15) Bahramikia, S., and Yazdanparast, R. (2013) Inhibition of human islet amyloid polypeptide or amylin aggregation by two manganese-salen derivatives. *Eur. J. Pharmacol.* 707 (1–3), 17–25.
- (16) Wang, L., Zhu, S., Lu, T., Zhang, G., Xu, J., Song, Y., Li, Y., Wang, L., Yang, B., and Li, F. (2016) The effects of a series of carbon dots on fibrillation and cytotoxicity of human islet amyloid polypeptide. *J. Mater. Chem. B* 4 (28), 4913–4921.
- (17) Yousaf, M., Huang, H., Li, P., Wang, C., and Yang, Y. (2017) Fluorine functionalized graphene quantum dots as inhibitor against hIAPP amyloid aggregation. ACS Chem. Neurosci. 8 (6), 1368–1377.
- (18) Xin, Y., Wang, X., Luo, L., and Meng, F. (2018) Conformation-dependent manipulation of human islet amyloid polypeptide fibrillation by shiitake-derived lentinan. *ACS Appl. Mater. Interfaces* 10 (37), 31069–31079.
- (19) Meng, Q.-Y., Wang, H., Cui, Z.-B., Yu, W.-G., and Lu, X.-Z. (2020) Chitosan Oligosaccharides Attenuate Amyloid Formation of hIAPP and Protect Pancreatic β -Cells from Cytotoxicity. *Molecules* 25 (6), 1314.
- (20) Mishra, A., Misra, A., Vaishnavi, T. S., Thota, C., Gupta, M., Ramakumar, S., and Chauhan, V. S. (2013) Conformationally restricted short peptides inhibit human islet amyloid polypeptide (hIAPP) fibrillization. *Chem. Commun.* 49 (26), 2688–2690.
- (21) Wang, L., Lei, L., Li, Y., Wang, L., and Li, F. (2014) A hIAPP-derived all-d-amino-acid inhibits hIAPP fibrillation efficiently at membrane surface by targeting α -helical oligomeric intermediates. *FEBS Lett.* 588 (6), 884–891.
- (22) Tang, Y., Zhang, D., Zhang, Y., Liu, Y., Gong, X., Chang, Y., Ren, B., and Zheng, J. (2020) Introduction and Fundamentals of Human Islet Amyloid Polypeptide Inhibitors. *ACS Applied Bio Materials* 3 (12), 8286–8308.
- (23) Haffner, S. M., Lehto, S., Rönnemaa, T., Pyörälä, K., and Laakso, M. (1998) Mortality from coronary heart disease in subjects with type 2 diabetes and in nondiabetic subjects with and without prior myocardial infarction. N. Engl. J. Med. 339 (4), 229–234.
- (24) Laakso, M. (1997) Epidemiology of macrovascular disease in diabetes. J. Diabetes Rev. 5, 294–315.

- (25) Kannel, W. B., and McGee, D. L. (1979) Diabetes and cardiovascular disease: the Framingham study. *JAMA, J. Am. Med. Assoc.* 241 (19), 2035–2038.
- (26) Hu, F. B., Stampfer, M. J., Haffner, S. M., Solomon, C. G., Willett, W. C., and Manson, J. E. (2002) Elevated risk of cardiovascular disease prior to clinical diagnosis of type 2 diabetes. *Diabetes Care* 25 (7), 1129–1134.
- (27) Manson, J. E., Colditz, G. A., Stampfer, M. J., Willett, W. C., Krolewski, A. S., Rosner, B., Arky, R. A., Speizer, F. E., and Hennekens, C. H. (1991) A prospective study of maturity-onset diabetes mellitus and risk of coronary heart disease and stroke in women. *Arch. Intern. Med.* 151 (6), 1141–1147.
- (28) Stamler, J., Vaccaro, O., Neaton, J. D., and Wentworth, D. (1993) Diabetes, other risk factors, and 12-yr cardiovascular mortality for men screened in the Multiple Risk Factor Intervention Trial. *Diabetes Care 16* (2), 434–444.
- (29) Laakso, M. (1999) Hyperglycemia and cardiovascular disease in type 2 diabetes. *Diabetes* 48 (5), 937–942.
- (30) Ashburn, T. T., and Thor, K. B. (2004) Drug repositioning: identifying and developing new uses for existing drugs. *Nat. Rev. Drug Discovery* 3 (8), 673–683.
- (31) Jiang, Q., and Lu, L. (2020) COVID-19: from crude oil to medical mask. ES Mater. Manuf 7, 1–3.
- (32) Shaikh, V. S., Nazeruddin, G. M., Bloukh, Y. I. S. S. H., Edis, Z., and Pathan, H. M. (2020) A Recapitulation of Virology, Modes of Dissemination, Diagnosis, Treatment, and Preventive measures of COVID-19: A Review. *Engineered Science* 10 (2), 11–23.
- (33) Ren, B., Zhang, M., Hu, R., Chen, H., Wang, M., Lin, Y., Sun, Y., Jia, L., Liang, G., and Zheng, J. (2017) Identification of a new function of cardiovascular disease drug 3-morpholinosydnonimine hydrochloride as an amyloid- β aggregation inhibitor. *ACS omega* 2 (1), 243–250.
- (34) Choi, S., Won, J.-S., Carroll, S. L., Annamalai, B., Singh, I., and Singh, A. K. (2018) Pathology of nNOS-expressing GABAergic neurons in mouse model of Alzheimer's disease. *Neuroscience* 384, 41–53.
- (35) Kumari, A., Sharma, R., Shrivastava, N., Somvanshi, P., and Grover, A. (2020) Bleomycin modulates amyloid aggregation in β -amyloid and hIAPP. *RSC Adv.* 10 (43), 25929–25946.
- (36) Wang, Q., Yu, X., Patal, K., Hu, R., Chuang, S., Zhang, G., and Zheng, J. (2013) Tanshinones inhibit amyloid aggregation by amyloid- β peptide, disaggregate amyloid fibrils, and protect cultured cells. ACS Chem. Neurosci. 4 (6), 1004–1015.
- (37) Mei, Z., Yan, P., Situ, B., Mou, Y., and Liu, P. (2012) Cryptotanshinione inhibits β -amyloid aggregation and protects damage from β -amyloid in SH-SY5Y cells. *Neurochem. Res.* 37 (3), 622–628.
- (38) Berstein, L. M. (2012) Metformin in obesity, cancer and aging: addressing controversies. *Aging* 4 (5), 320.
- (39) Nawarskas, J. J., and Shephard, E. A. (2020) Tafamidis: A Novel Treatment for Transthyretin Amyloid Cardiomyopathy. *Cardiology in review* 28 (3), 156–160.
- (40) Mossuti, E., Nigro, P., Diene, G., and Petralito, A. (1976) Use of cloridarol in coronary insufficiency. *Minerva medica* 67 (21), 1394–1397.
- (41) Kanehisa, M., Furumichi, M., Tanabe, M., Sato, Y., and Morishima, K. (2017) KEGG: new perspectives on genomes, pathways, diseases and drugs. *Nucleic Acids Res.* 45 (D1), D353–D361.
- (42) Kamal, M., Shakya, A. K., and Jawaid, T. (2011) Benzofurans: a new profile of biological activities. *International Journal of Medical and Pharmaceutical Sciences* 1 (3), 1-15.
- (43) Asif, M. (2016) Mini review on important biological properties of benzofuran derivatives. *J. Anal Pharm. Res.* 3 (2), 00050.
- (44) López, L. C., Varea, O., Navarro, S., Carrodeguas, J. A., Sanchez de Groot, N., Ventura, S., and Sancho, J. (2016) Benzbromarone, quercetin, and folic acid inhibit amylin aggregation. *Int. J. Mol. Sci.* 17 (6), 964.

- (45) Cheng, B., Gong, H., Li, X., Sun, Y., Chen, H., Zhang, X., Wu, Q., Zheng, L., and Huang, K. (2013) Salvianolic acid B inhibits the amyloid formation of human islet amyloid polypeptideand protects pancreatic beta-cells against cytotoxicity. *Proteins: Struct., Funct., Genet.* 81 (4), 613–621.
- (46) Alkahtane, A. A., Alghamdi, H. A., Almutairi, B., Khan, M. M., Hasnain, M. S., Abdel-Daim, M. M., Alghamdi, W. M., and Alkahtani, S. (2021) Inhibition of human amylin aggregation by Flavonoid Chrysin: An in-silico and in-vitro approach. *Int. J. Med. Sci.* 18 (1), 199.
- (47) Durairajan, S. S. K., Yuan, Q., Xie, L., Chan, W.-S., Kum, W.-F., Koo, I., Liu, C., Song, Y., Huang, J.-D., Klein, W. L., and Li, M. (2008) Salvianolic acid B inhibits $A\beta$ fibril formation and disaggregates preformed fibrils and protects against $A\beta$ -induced cytotoxicty. *Neurochem. Int.* 52 (4–5), 741–750.
- (48) Saito, S., Yamamoto, Y., Maki, T., Hattori, Y., Ito, H., Mizuno, K., Harada-Shiba, M., Kalaria, R. N., Fukushima, M., and Takahashi, R. (2017) Taxifolin inhibits amyloid- β oligomer formation and fully restores vascular integrity and memory in cerebral amyloid angiopathy. *Acta neuropathologica communications* 5 (1), 1–16.
- (49) Williamson, J. A., and Miranker, A. D. (2007) Direct detection of transient α -helical states in islet amyloid polypeptide. *Protein Sci.* 16 (1), 110–117.
- (50) Lam, Y. P. Y., Wootton, C. A., Hands-Portman, I., Wei, J., Chiu, C. K. C., Romero-Canelon, I., Lermyte, F., Barrow, M. P., and O'Connor, P. B. (2020) Determination of the Aggregate Binding Site of Amyloid Protofibrils Using Electron Capture Dissociation Tandem Mass Spectrometry. J. Am. Soc. Mass Spectrom. 31 (2), 267–276.
- (51) Liu, Y., Zhang, D., Zhang, Y., Tang, Y., Xu, L., He, H., Wu, J., and Zheng, J. (2020) Molecular Dynamics Simulations of Cholesterol Effects on the Interaction of hIAPP with Lipid Bilayer. *J. Phys. Chem. B* 124 (36), 7830–7841.
- (52) MacKerell, A. D., Jr, Bashford, D., Bellott, M., Dunbrack, R. L., Jr, Evanseck, J. D., Field, M. J., Fischer, S., Gao, J., Guo, H., Ha, S., et al. (1998) All-atom empirical potential for molecular modeling and dynamics studies of proteins. *J. Phys. Chem. B* 102 (18), 3586–3616.
- (53) Luca, S., Yau, W.-M., Leapman, R., and Tycko, R. (2007) Peptide Conformation and Supramolecular Organization in Amylin Fibrils: Constraints from Solid-State NMR. *Biochemistry* 46 (47), 13505–13522.
- (54) Phillips, J. C., Braun, R., Wang, W., Gumbart, J., Tajkhorshid, E., Villa, E., Chipot, C., Skeel, R. D., Kalé, L., and Schulten, K. (2005) Scalable molecular dynamics with NAMD. *J. Comput. Chem.* 26 (16), 1781–1802.